applied sciences

MDPI

Article

Human Respiration and Motion Detection Based on Deep Learning and Signal Processing Techniques to Support Search and Rescue Teams

Özden Niyaz [1,*], Mehmet Ziya Erenoğlu [2], Ahmet Serdar Türk [1], Sultan Aldirmaz Colak [3], Burcu Erkmen [1] and Nurhan Türker Tokan [1]

[1] Department of Electronics and Communication Engineering, Yildiz Technical University, Istanbul 34220, Türkiye; asturk@yildiz.edu.tr (A.S.T.); bkapan@yildiz.edu.tr (B.E.); nturker@yildiz.edu.tr (N.T.T.)
[2] Faculty of Engineering and Natural Sciences, Bahçeşehir University, Istanbul 34349, Türkiye; mehmetziya.erenoglu@bau.edu.tr
[3] Department of Electronics and Communication Engineering, Kocaeli University, Kocaeli 41001, Türkiye; sultan.aldirmaz@kocaeli.edu.tr
* Correspondence: oniyaz@yildiz.edu.tr

Abstract: The quick and effective detection of humans trapped under debris is crucial in search and rescue operations. This study explores the use of antennas operating within the 150–650 MHz frequency range to identify human respiration and movement under building wreckage. A debris model consisting of construction materials was generated at the laboratory, and attenuation characteristics were observed to set ideal operating frequencies. Time-dependent transmission coefficient data were collected over 20 s and processed using short-time Fourier transform, wavelet transform, and empirical mode decomposition for time-frequency analysis. To enhance signal clarity, denoising techniques were applied before the radar signals were categorized into three classes: empty debris, human respiration, and human movement. Generative adversarial networks augmented environmental noise data to enrich training datasets comprising nine subsets. Deep learning models, including temporal convolutional networks, long short-term memory, and convolutional neural networks, were employed for classification. Hyperparameter optimization via random search further refined model performance. Results indicate that the convolutional neural networks using short-time Fourier transform data consistently achieved the highest classification accuracy across subsets. These findings demonstrate the potential of combining radar with deep learning for reliable human detection under debris, advancing rescue efforts in disaster scenarios.

Keywords: deep learning; remote sensing; search and rescue radar

check for updates

Academic Editor: Leo K. Cheng

Received: 5 January 2025
Revised: 9 February 2025
Accepted: 13 February 2025
Published: 17 February 2025

Citation: Niyaz, Ö.; Erenoğlu, M.Z.; Türk, A.S.; Colak, S.A.; Erkmen, B.; Tokan, N.T. Human Respiration and Motion Detection Based on Deep Learning and Signal Processing Techniques to Support Search and Rescue Teams. *Appl. Sci.* **2025**, *15*, 2097. https://doi.org/10.3390/app15042097

Copyright: © 2025 by the authors. Licensee MDPI, Basel, Switzerland. This article is an open access article distributed under the terms and conditions of the Creative Commons Attribution (CC BY) license (https://creativecommons.org/licenses/by/4.0/).

1. Introduction

After a natural disaster, the rapid and effective rescue of trapped individuals within collapsed structures has paramount importance since the window of survival in such scenarios is limited [1]. Efficient procedures and the timely deployment of appropriate rescue resources are crucial for reaching survivors within the critical timeframe [2–4]. Technological tools, such as acoustic detectors, trained canines, snake camera robots, and high-sensitivity microphones, are used by search and rescue teams to detect survivors. However, each method possesses inherent limitations when deployed in a complex debris field [5]. Thus, it is imperative to use a reliable sensing device that can detect living victims

in the debris. Over the years, there has been a growing interest in utilizing remote sensing technologies for the detection of living humans, especially as part of search and rescue operations [6]. Radar technology has emerged as a particularly effective tool for this purpose, enabling the detection of human breathing and movement under debris [7]. By analyzing the reflected electromagnetic waves from the debris area, radar devices can distinguish the presence of objects in the environment, including individuals trapped in collapsed structures. Specialized radar technology further improves this capability by detecting vital signs such as heartbeats, breathing, and body movements under debris conditions [8,9]. Various radar types, such as pulse radar, continuous wave radar, and Doppler-based methods, have been used for detecting trapped victims in collapsed buildings [10–13]. Recently, ultra-wideband (UWB) radar systems have emerged as promising tools for penetrating debris and detecting vital signs such as respiration and movement responses. The integration of Doppler techniques with UWB radars has enabled the detection of micro-movements indicative of living individuals [14–16]. Despite the challenges associated with higher frequencies and penetration depth, UWB radar systems have demonstrated impressive performance in detecting individuals buried under debris, thus enhancing the efficiency of the search and rescue teams significantly [17–20].

The heterogeneity of the environment is the main difficulty that radar systems face. Building wreckage is a heterogeneous environment with various structural components, such as concrete, wood, cement, aggregate, and brick, each of which has different compositions and positioning [21]. This heterogeneity causes scattering of the electromagnetic waves, thereby reducing the detection depth. Prior work, such as [22], has demonstrated high accuracy in detecting weak ranging signals in FoV scenarios using mmWave radar at 60–64 GHz. This method leverages range profile variations and clutter removal techniques to identify a human presence before proceeding to respiration monitoring. In [22], by using Alpha filtering in the Fourier transform of the FMCW intermediate signal, the environmental clutter is significantly reduced, and weak signals from the subject can be observed. The study shows that the detection rate is increased, especially when the object sits behind the radar. Furthermore, several studies highlight the significance of reducing clutter and mitigating signal attenuation through dense materials in post-disaster scenarios, especially for locating survivors and critical assets [23,24]. These approaches employ specialized radar methods and advanced signal processing algorithms to enhance detection accuracy under extreme conditions [25]. Additionally, there is a further complication in signal detection due to the clutter of moving objects, which causes difficulty in discriminating human movement from noise [26]. This issue can be addressed by denoising the stationary clutter through advanced signal processing techniques [27].

The detection of a human presence within the debris is still an important scientific and technological issue that requires additional solutions with higher detection accuracy and depth. Measurement procedures and signal processing techniques should be designed to minimize false alarms and maximize the probability of correct detection. Signal processing is vital for detection processes, because analyzing the frequency content of a signal via the Fourier transform (FT) yields deeper insights into its characteristics [28,29]. Short-time Fourier transform (STFT) and wavelet transform (WT) are particularly advantageous in this regard because they simultaneously provide time and frequency information about the signal [30,31]. Such time–frequency analysis methods are widely used for respiratory (vital sign) detection, where signals typically exhibit periodic changes within a narrow frequency range of approximately 0.1–0.5 Hz [32,33]. Different from these methods, the signal can be decomposed into different signal components in the time domain by using empirical mode decomposition (EMD) and variational mode decomposition (VMD) methods. In the literature, STFT analysis was performed on UWB impulse radar signals in [34], and

WT and EMD methods were both applied to Doppler radar signals in [35]. In addition, EMD has been used in different studies [36–38]. EMD was used for Doppler radar signals to identify the arm swinging, breathing, and torso bending movements of humans in debris in [38]. Related studies have performed wavelet analysis of respiratory muscles' EMG signals [39], extracted respiratory information from ECG signals using EMD [40], and employed EMD-based methods for predicting respiratory motion [41]. These works underscore the versatility of advanced signal decomposition techniques in processing physiological signals across various contexts and further enrich the discussion on their applicability for detecting and characterizing respiratory activity. A newer decomposition method, VMD , was also performed on UWB and FMCW radar signals in [42,43], respectively. To reduce interference and improve the signal-to-noise ratio (SNR) of the signals, state–space methods comprising complex signal demodulation (CSD) and arctangent demodulation (AD) techniques have been developed [44]. A radar-based system, employing a hidden semi-Markov model, highlights the potential of radar technology in capturing heart sounds in the phonocardiograph and radar data [45]. An advanced template matching (ATM) algorithm is utilized for heartbeat detection. Additionally, a hidden Markov model has been employed to detect chest movement due to respiration using impulse radio UWB systems for contactless noninvasive respiratory monitoring [46]. Research also focuses on wireless detection of human respiratory parameters using multi-peak detection of the pulse regulation method with a chest strap sensor [47]. Furthermore, respiratory rate measurement has been conducted using a single wireless continuous wave Doppler radar life signal detection system [48]. In a study on the UWB radar systems, FFT and S-transform were employed to detect and identify human targets through walls [49]. One study [50] carried out human movement detection through walls using a synthetic data set as well as an experimental data set collected with UWB radar. The curvelet transform was developed to eliminate background noise signals, and FFT and the Hilbert–Huang transform were employed to obtain vital sign frequencies.

In addition to all of the above-mentioned techniques, artificial intelligence (AI) holds significant promise for advancing the capabilities of respiration and movement detection [51]. An innovative approach using AI-based methods to detect human respiration under debris is presented in [52], which uses a phantom model generated in CST Microwave Studio. By generating simulation-based electromagnetic data and using ANN-based surrogate models, respiratory-related movements are detected. A custom neural network is proposed for detecting diseases using two data sets collected from a breathing belt and a radio sensor [53]. Radar technology facilitates robust human activity recognition in challenging environments, including those with high noise [54], aligning with research endeavors focused on the application of phase and frequency analysis for the identification of vital signs in high-noise settings. In particular, a frequency-shift keying radar in the 2.45-GHz band has been proposed for accurate vital sign detection [55]. Recent innovations in radar detection techniques, which integrate advanced signal processing and AI, have demonstrated significant improvements in tasks such as fall detection and activity classification [56]. Additionally, deep convolutional autoencoders have been employed for denoising in a near-field situation with moving objects using FMCW radar [57]. Doppler radars identify life signs for earthquake rescue with micro-Doppler signatures, using EMD signals as input to the binary classifier [38]. Contactless real-time heartbeat detection via 24 GHz continuous-wave Doppler radar using simple feedforward artificial neural networks (ANNs) has been achieved [58]. A diverse range of applications utilizing convolutional neural networks (CNNs) includes a movement detection system employing a continuous-wave Doppler radar sensor for detecting coughing and other gestures, multiple stationary human target detection in through-wall UWB radar, and real-time monitoring

of vital signs based on impulse radio UWB radar during sleep [59–61]. A variety of deep learning (DL) techniques have been employed for non-contact physiological monitoring, including an efficient heart rate measurement system that utilizes medical radar and LSTM neural network, as well as a deep neural network (DNN) model capable of classifying respiratory signals into inhalation and exhalation using non-contact UWB radar [62,63]. The real-world application of measuring earthquake rubble involves detecting human vital signs using ground penetrating radar, with future research focusing on signal processing techniques [64]. Additionally, spatiotemporal processing for the remote sensing of trapped victims using 4D imaging radar in real debris has not utilized AI-enabled methods in either case [65]. Considering all these recent studies, employing AI for detecting and classifying human respiration and movement under debris presents a novel approach.

In this work, a debris model was constructed in a laboratory environment equipped with a UWB bi-static radar system to estimate the presence of living humans. Since the debris model, which presents a heterogeneous environment with various structural components, makes the signals more complex due to the scattering of electromagnetic waves caused by reflections and moving objects, preprocessing algorithms are needed for meaningful signal detection. Preprocessing techniques such as STFT, WT, and EMD are used to distinguish human motion from noise/clutter signals. The measurements show that the measured signal of the empty debris is different than the case in which a breathing or moving human subject is in the debris model. A raw data set was created with human subjects of different ages, genders, and heights and in different lying orientations. The number of samples was increased with a data augmentation technique (using generative adversarial nets; GANs), and the final form of the data set was obtained by employing signal processing techniques. Afterward, DL techniques such as LSTM, CNN, and temporal convolutional network (TCN) architectures were applied to the signal to detect the presence of the human.

This paper is organized as follows: In Section 2, the system definition, which includes radar components and the physical debris model, is given. In Section 3, the data set is explained in detail. Section 4 presents preprocessing operations and time–frequency analysis methods. AI and DL techniques are given in Section 5, and the classification results are demonstrated in Section 6. Finally, the paper is concluded in Section 7.

2. System Definition

The components of the system, including the antennas and the physical debris model created with real materials, are explained in this section.

2.1. Components of the Radar System

A UWB bistatic radar approach was used for determining the respiration and movement of the human. Considering the attenuation characteristics of the building construction materials, such as concrete, brick, marble, and wood, a wideband operating radar that covers the 150–650 MHz frequency band was preferred. The signal attenuates rapidly within dense materials such as concrete, especially at high frequencies. Thus, operation at low frequencies is required to reach lengthy distances. However, for the signal to pass through the iron grids of the building, a higher frequency operation is required. The undetermined and heterogeneous nature of the debris requires the usage of the wideband radar system.

The radar system consisted of a 1.3 GHz vector network analyzer (VNA), a power amplifier, a receiver, and a transmitter antenna. The dynamic range of the 2-Port VNA was 135 dB (10 Hz intermediate frequency bandwidth; IFBW), and the output power adjustment range was between −55 dBm and +3 dBm. RF coaxial cables were used for the connections with the antennas. N-type to SMA adapters were used for connecting the coaxial cables to the VNA ports. The wide band amplifier has high output power (+26 dBm)

and high flat gain (27 ± 2 dB typ.). The receiving and transmitting antennas were linearly polarized bowtie antennas operating in the 150–650 MHz band. The transmitting antenna was connected to the first port of the VNA, whereas the receiving antenna was connected to the second port. The concept of the human detection radar system is demonstrated in Figure 1. The control interface, which was compiled in MATLAB 2023b, was used to follow the measurements at each step. First, the system determined the ideal operating frequencies automatically by observing the attenuation characteristics of the debris. The transmission coefficient variation was measured as the function of frequency. Three frequencies that exhibit low-loss characteristics were chosen by the system. Afterward, the amplified signal at the chosen frequencies was sent to the physical debris model, which was constructed in the laboratory by the transmitting antenna. The signal received by the receiving antenna was transmitted to the second port of the VNA. During the measurements, a human subject lies within the corrugated pipe along the *z*-axis. The measured signal was processed, and a result that provides information about the condition of the human within the corrugated pipe was obtained by the radar control interface.

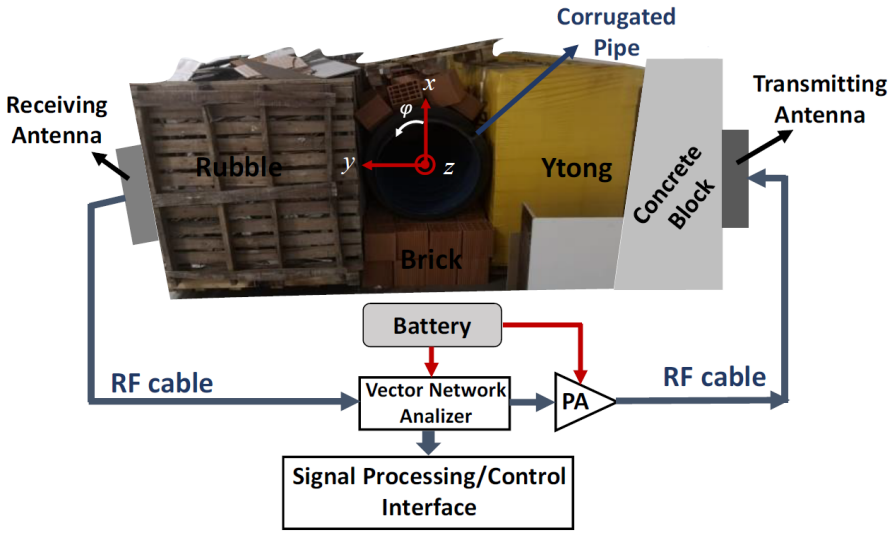


Figure 1. Radar based human detection system.

2.2. The Physical Debris Model

To evaluate the performance of the AI-based human detection system, a debris model was constructed in the laboratory. The main construction components of a building were used in the debris model. The constructed debris model comprises concrete blocks, autoclaved aerated concrete (AAC), brick, wood, and rubble. The concrete block with 30 cm thickness was part of a 6 m × 4 m concrete wall and contained two grids of iron bars that were separated from each other by 20 cm. The dimensions of the AAC material and rubble pile were 75 × 135 × 130 cm^3 and 113 × 135 × 130 cm^3 (width × length × height), respectively. A corrugated pipe with a 60 cm inner diameter was placed between the rubble and AAC blocks. The corrugated pipe, which is resistant to heavy loads, was used to ensure the safety of the human subject during the measurements. The overall width of the debris model was 298 cm. The debris model is shown in Figure 2a, while its side view is presented in Figure 2b.



Figure 2. Physically constructed debris model in our laboratory. (**a**) Front view. (**b**) Side view.

3. Data Set

The characteristics of the measured signals for different scenarios are defined in this section. The features of individuals, including age, height, and weight are summarized in Table 1. Henceforth, these participants will be referred to as subjects. Five women and 15 men took part in the measurements as the subjects inside the corrugated pipe. Time-dependent measurements were conducted on the real debris model in the laboratory environment. Measurements of each subject were completed for six different angular positions depending on the ϕ angle demonstrated in Figure 1. When $\phi = 0^\circ$, the subject faced towards the x-axis. For each ϕ orientation, signal variation for three different respiration-movement states was recorded. External noise was minimized during the measurements by keeping the measurement setup in a movement-free zone. In addition, recordings of the empty debris were made under various environmental noises generated due to external movements. Details of the recorded signals are as follows:

- Twenty seconds of respiration of the subject in the debris with environmental noise;
- Twenty seconds of respiration of the subject in the debris;
- Twenty seconds of movement of the subject in the debris.

Measurements were taken for the environment analysis at the three distinct highest frequencies—210 MHz, 332.5 MHz, and 405 MHz—where signal transmission was achieved with the highest gain. Measurement at each frequency lasted 20 s for each ϕ orientation ($\phi \in \{0^\circ, 45^\circ, 90^\circ, 135^\circ, 180^\circ, 270^\circ\}$). The sampling frequency was set to 80 Hz. Thus, each recorded signal contains 1600 samples. The recording duration was approximately 45 min to 1 h for each subject. DC components were removed from the signals to expose variations in amplitude and phase. Table 2 demonstrates the main features of the entire data set.

As a demonstration of the signal characteristic recorded from the measurement setup, phase and magnitude variations of the signal at 405 MHz frequency are given in Figure 3 as a function of the recording time. The solid blue line represents the case in which the corrugated pipe placed inside the debris was empty, whereas the red dashed and black dotted lines represent the case in which the subject inside the corrugated pipe respired or moved. If the magnitude and phase responses are compared, it can be concluded that the movement of the chest or body affects the phase signal more predominantly than the magnitude signal. The respiration signal follows a sinusoidal characteristic, the maximum value of which is much lower than the maximum of the signal derived from the movement of the body.

Table 1. Main characteristics of the subjects inside the debris.

Gender	Height Range [cm]	Weight Range [kg]	Age Range	Number of Subjects
Female	160–177	58–85	27–50	5
Male	170–190	62–115	19–31	15

Table 2. Main features of the data set from the measurement setup (Mag acronym represents magnitude).

Orientation (ϕ)	Num. of Subjects	Frequencies [MHz]	Records	Duration [sec]	Sampling Freq. [Hz]	Signal Size (for Each ϕ Orientation)
0°, 45°, 90°, 135°, 180°, 270°	20	210	Mag/Phase	20	80	20×1600
0°, 45°, 90°, 135°, 180°, 270°	20	332.5	Mag/Phase	20	80	20×1600
0°, 45°, 90°, 135°, 180°, 270°	20	405	Mag/Phase	20	80	20×1600

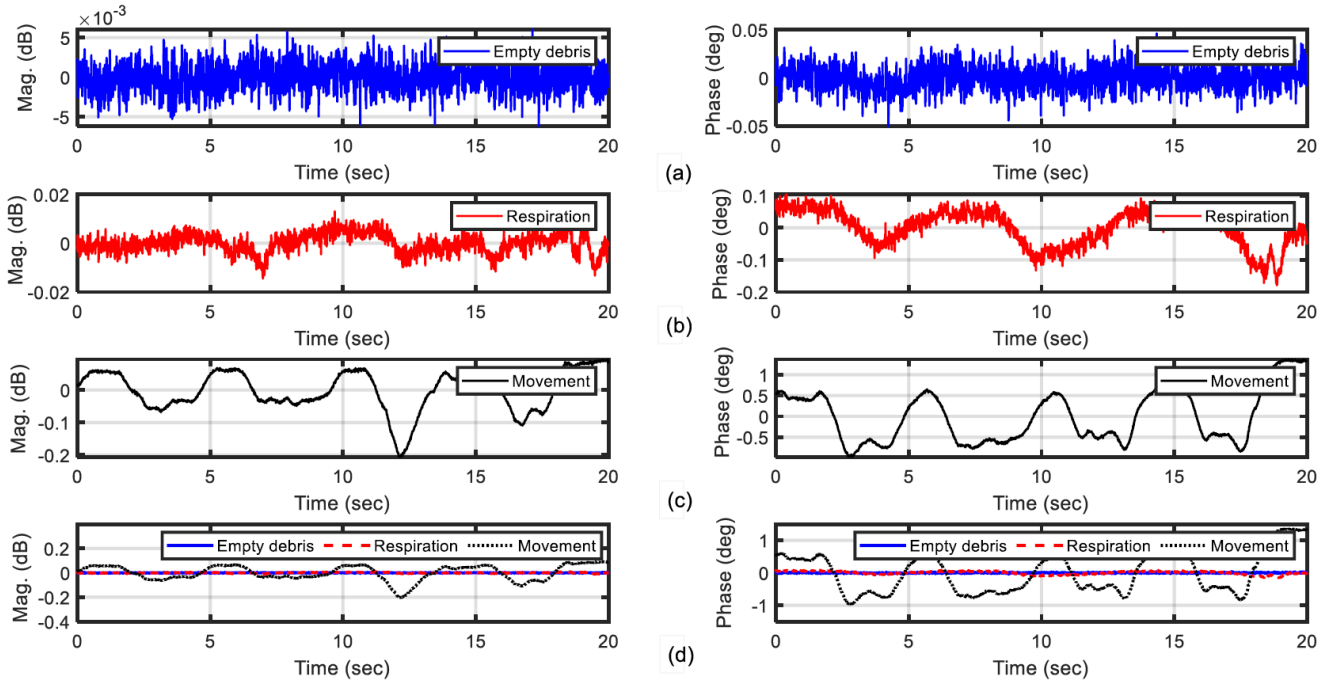
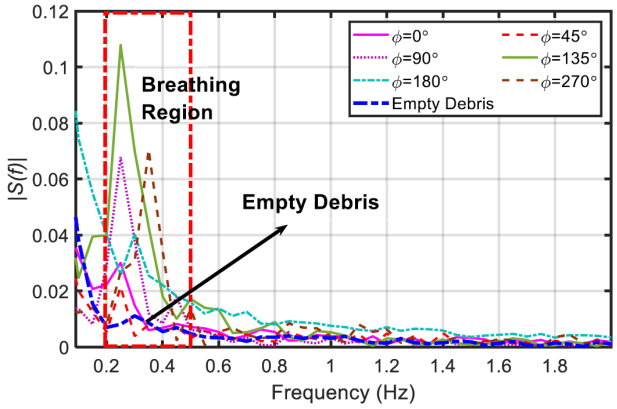


Figure 3. Variation of the raw measured magnitude and phase of S_{21} signals at 405 MHz for different scenarios (**a**) Empty debris. (**b**) Respiration. (**c**) Movement. (**d**) Combined plots.

To assess the impact of various parameters on detection performance, we conducted measurements at different frequencies (210 MHz, 332.5 MHz, and 405 MHz) and subject orientation angles (0°, 90°, and 180°). Our results show that the lowest frequency (210 MHz) provides more stable STFT results in noisy environments, while higher frequencies exhibit greater variation. Similarly, when the subject is oriented at 180°, the amplitude of the STFT signal significantly decreases, leading to lower detection rates. These findings underscore the importance of carefully selecting both frequency and orientation to achieve robust respiratory monitoring.

Figure 4a illustrates the magnitude of the FT of the phase of the S_{21} signals measured at 405 MHz for different subject orientation angles within the debris. The magnitude of this signal is denoted by $|S(f)|$, providing insights into how orientation affects the detected signal strength.

Two important conclusions can be deduced from this figure. The first is that the FT magnitude ($|S(f)|$) of the signal measured when the debris is empty is considerably lower than when there is a person inside. The second is that the frequency of the maximum signal peak varies between 0.2 and 0.4 Hz depending on the orientation of the subject in the debris. The statistical features of the data set are summarized in Figure 4b as well. By observing the values of statistical features, it can be concluded that the data sets recorded in different conditions can be distinguished from each other. Furthermore, the discriminability of the average variance and standard deviation of the phase information is more prominent compared to amplitude information. Therefore, the phase signal is preferred for respiration and movement detection. While average values provide general information about the data set, not all vectors within it exhibit common characteristics. Hence, the usage of signal preprocessing and artificial intelligence is necessary for respiration and movement detection in real debris scenarios.



(**a**)

Frequency [MHz]	Dataset		Average Standard Deviation
210	Phase	Empty	0.017
		Respiration	0.026
		Movement	0.830
	Magnitude	Empty	0.004
		Respiration	0.003
		Movement	0.129
332.5	Phase	Empty	0.020
		Respiration	0.048
		Movement	1.460
	Magnitude	Empty	0.003
		Respiration	0.009
		Movement	0.220
405	Phase	Empty	0.015
		Respiration	0.069
		Movement	0.906
	Magnitude	Empty	0.002
		Respiration	0.009
		Movement	0.216

(**b**)

Figure 4. Analysis of the S_{21} signals measured for different orientation angles of the subject: (**a**) FT of the measured phase of S_{21} signals at 405 MHz. (**b**) Average standard deviation of the phase and magnitude at different frequencies.

4. Preprocessing of the Measured Data

The human trapped under the debris generates a time-varying signal caused by physical movements like breathing. The detection of such a signal is a positive indication of the potential presence of a survivor. Although the movement area of the trapped survivors within the debris is narrow, they still create a movement on the body surface of approximately 1–4 mm while they breathe. Additionally, there can be body movements of a few centimeters. The amplitude and phase of the reflected signal change according to the movement of the survivor, which allows for motion detection when a microwave is spread out into the debris. However, as well as recording the vital signal of the human, the background noise is also measured. Thus, preprocessing of the signal to increase the probability of detection (PD) is indispensable. In the following subsection, a brief overview of denoising, STFT, CWT, and EMD is provided. In addition, GANs used for data augmentation in preprocessing techniques are presented. The distribution of the measured signal energy in the time–frequency plane are presented, along with the corresponding analysis parameters.

4.1. Denoising

The measured time-varying signal includes the movement of the victim under the debris, as well as undesired signals around the measurement area. These undesired signals can significantly degrade detection performance by masking the subtle motion patterns of the victim, potentially leading to missed detections and higher false alarm rates [66,67].

Therefore, a robust and targeted filtering of these components is essential to enhance the reliability and accuracy of the detection system. To increase the PD and reduce the probability of false alarms (FAs), signal components caused by the chaotic environment in the region and the noise that it creates should be filtered out. Wavelet-based noise reduction is a suitable solution for this purpose [68]. The orthogonality and tight support of the wavelet function result in good performance for signal denoising. This method aims to separate noise and signal by analyzing the frequency components of the signal at different scales. It provides a multi-resolution analysis that can decompose a signal into different frequency components at various resolutions. This capability enables the identification and removal of the noise at different scales and increases the clarity of the underlying signal among chaotic environmental conditions. It allows rapid processing of large data sets, which contributes to the timely and accurate detection of survivors in our case. The Wavelet Signal Denoiser tool in MATLAB2023 was used for the denoising of the measured data [69]. The 8th-order Daubechies wavelet was used as the mother wavelet. The optimal decomposition level was determined to be seven, and the hard threshold rule was chosen.

4.2. STFT Analysis of the Measured Signal

The short-time Fourier transform is a powerful tool for time–frequency analysis. Unlike the well-known Fourier transform (FT), it presents frequency content together with time information. The STFT can be thought of as a 2D image. Each column of this image contains the FT of the signal bounded by a window function. The window function is then shifted slightly on the signal, and the other columns of the STFT are formed by calculating the FT operation again for the received signal portion. The STFT can be calculated by Equation (1):

$$STFT_x(m,k) = \sum_{n=-\infty}^{\infty} x[n]w[n-m]e^{-\frac{2\pi kn}{N}}, \quad (1)$$

where $x[n]$ and $w[n]$ are the discrete signal vector and the window function, respectively. N represents the FFT length. The frequency resolution improves as N increases. Using FFT, the signal's frequency content between $-f_s/2$ and $f_s/2$ is obtained ($\pm$40 Hz), where f_s denotes the sampling frequency. Only the positive and low-frequency parts of the STFT are considered in the classification for two reasons: 1. The absolute value of the STFT images is the same for positive and negative frequencies. Thus, the data size can be reduced by taking only the positive part. 2. Since the aim was to detect whether the debris was empty or not, the detection of respiration and motion was required. Since the respiration frequency ranges between 0.2 and 0.5 Hz, it was sufficient to focus on the low-frequency range (0–5 Hz).

The STFT analysis was performed using a moving window with a constant length (L). The main signal was divided into a set of segments, and each segment was refined using the conventional FFT algorithm. The resolution of the STFT depends on the selection of the window function, overlapping value, and FFT length. In this study, N, L, and overlapping value were set to 1024, $4f_s$, and $5f_s/8$, respectively. A Hamming window was employed to select the signal portion, while various window functions were used to address the issue of spectral leakage in the STFT process.

Figure 5 represents the STFT images (with dB values) of the measured respiration and movement phase data from a subject with different orientations in the debris. Similar to Figure 4, the STFT values were quite small for empty debris. Additionally, the signal energy changed significantly over the 0–5 Hz frequency range, depending on the orientation of the subject. The figure also shows that the energy was more localized at lower frequencies compared to high-frequency STFT values.

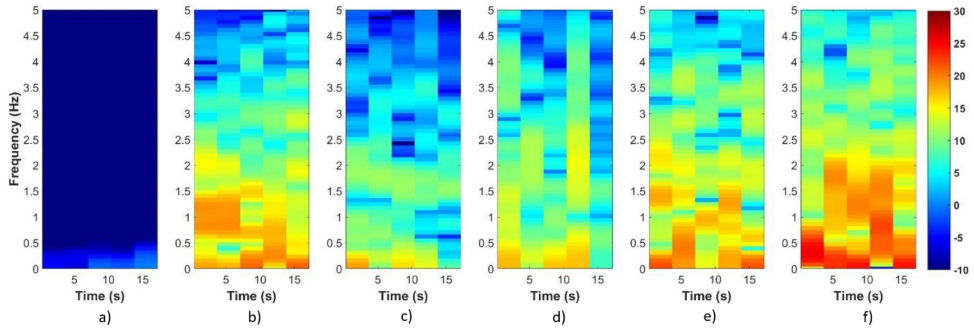


Figure 5. STFT images of the measured signal for 20 s: (**a**) when the debris is empty. A subject is inside the debris with orientation of: (**b**) $\phi = 0°$. (**c**) $\phi = 45°$. (**d**) $\phi = 90°$. (**e**) $\phi = 180°$. (**f**) $\phi = 270°$.

4.3. WT Analysis of the Measured Signal

Wavelet transform (WT) is another time–frequency analysis tool. Since the width of the window function—which remains constant throughout the transformation in STFT—constantly changes in the WT, the resolution of both time and frequency domains increases [70]. The mother wavelet function is both scaled and shifted during the transformation process. Mathematically, the continuous wavelet transform (CWT) is expressed by the following equation:

$$CWT_f(a,b) = \int_{-\infty}^{\infty} x(t) \frac{1}{\sqrt{a}} \psi\left(\frac{t-b}{a}\right) dt, \tag{2}$$

where ψ symbolizes the wavelet function, a represents the scale parameter that controls the width of the wavelet, and b represents the position parameter that determines the position of the wavelet on the signal.

Figure 6 presents CWT images of the signals that were analyzed by STFT in the previous subsection.

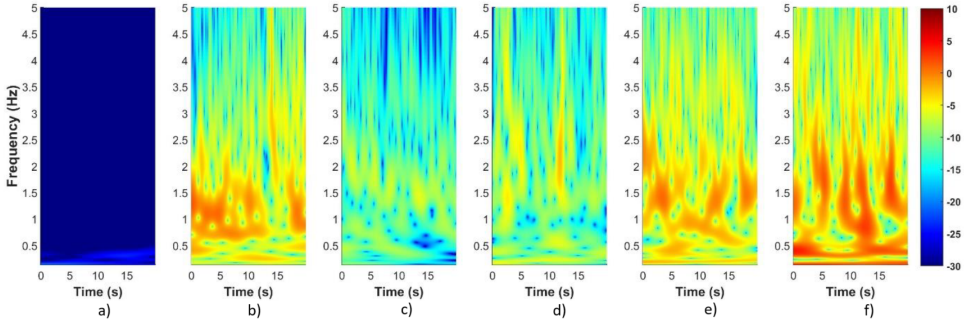


Figure 6. CWT images of the measured signal for 20 s : (**a**) when the debris is empty. A subject is inside the debris with orientation of: (**b**) $\phi = 0°$. (**c**) $\phi = 45°$. (**d**) $\phi = 90°$. (**e**) $\phi = 180°$. (**f**) $\phi = 270°$.

STFT employs a predefined window, the properties of which remain constant throughout the analysis, resulting in a fixed time–frequency resolution. This characteristic allows STFT to consistently capture changes in respiratory signals that typically occur within specific frequency bands. In contrast, the wavelet transform provides variable resolution, which, in some cases, may lead to information loss or inconsistencies in feature extraction. Additionally, the wavelet transform applies longer time windows for low-frequency components and shorter time windows for high-frequency components. While this adaptability can be beneficial, it may also obscure certain critical respiratory features, making them less distinguishable.

4.4. EMD Analysis of the Measured Signals

Empirical mode decomposition (EMD) provides time–frequency analysis by decomposing signals into component modes. Its adaptive and empirical nature also enables nonstationary and nonlinear processes to be dealt with. EMD highlights the instantaneous frequencies that express the frequency characteristics of each mode over time. This provides a detailed analysis of the frequency distribution of the signal. It decomposes a signal into a finite set of functions with different frequency components. In other words, the EMD method is based on the principle that any real-valued input signal consists of the sum of simple sub-signals that oscillate differently. Each of these sub-signals is called an intrinsic mode function (IMF), and each of these intrinsic modes represents a simple oscillation with the same number of extrema and zero-crossings [71,72].

In EMD analysis, a signal can be decomposed into many IMFs. IMFs with higher frequency and/or lower energy generally represent noise and unwanted signals [73]. Therefore, a high-frequency band component is obtained (IMF1) and subtracted from the signal. This process is repeated for other IMFs that have lower frequency band detection until the residual signal is lower than a threshold value. Therefore, as the IMF order (number) increases, the frequency content of the signal components decreases. In this study, the signal is first decomposed into eight IMFs. The FT of each IMF is calculated and represented by $\mathrm{IMF}_k(f)$. Then, the energy density between the frequency ranges of 0 and 1.3 Hz for the k^{th} IMF is calculated by Equation (3):

$$E_k = \frac{\sum_{f=0}^{1.3} |\mathrm{IMF}_k(f)|^2}{\sum_{f=0}^{5} |\mathrm{IMF}_k(f)|^2}, \tag{3}$$

where f denotes the frequency index, and the $\mathbf{E} = [E_1, E_2, \ldots, E_k]$ vector is obtained. Finally, four IMF indices, the E_k of which is greater than 0.07, are selected. If there are fewer than four IMF indices that satisfy this condition, the other IMFs are assumed to be zero vectors. The limits of summation in Equation (3) are determined considering the fact that the frequency components of the respiratory data are in the range of 0.1–0.5 Hz. Thus, we selected the four IMFs with the highest energy density between the 0 and 1.3 Hz frequency interval. According to Equation (3) and this IMF selection rule, IMFs 3, 4, 5, and 6 are selected. These IMFs construct a matrix with a size of $L \times 4$, where L represents the signal length of the IMFs.

The IMFs obtained for the signal of a moving subject with an orientation angle of $\phi = 0^\circ$ inside the debris are shown in Figure 7. It can be seen that the first two IMFs (IMF 3 and IMF 4) contain higher frequency components compared to IMF 5 and IMF 6.

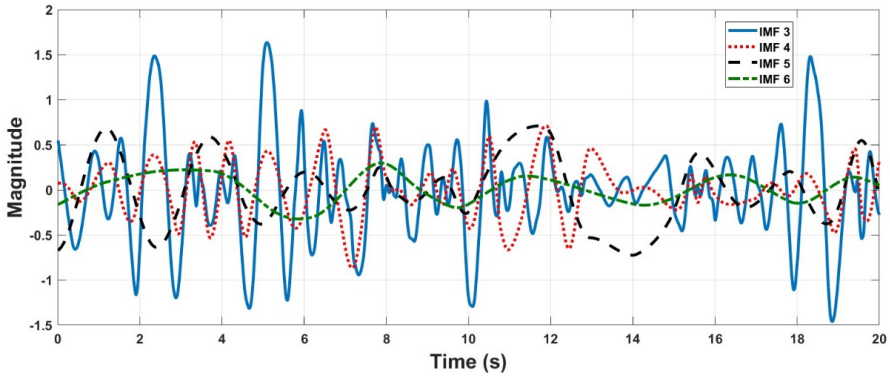


Figure 7. Selected IMFs of the EMD analysis for a measured signal of a moving subject inside the debris with $\phi = 0^\circ$ orientation angle.

4.5. Data Augmentation Using Generative Adversarial Networks

In our data set, the empty debris (noise) class initially contained only 20 real samples, which was significantly fewer than the respiration and movement classes. To address this imbalance and strengthen the model's ability to distinguish between classes, we leveraged GANs to augment the noise data. By synthesizing additional realistic noise samples, we created a more balanced data set that allowed the model to learn discriminative features effectively, helping mitigate potential bias and improve overall classification performance. The data set was augmented by generating synthetic samples, which increased the amount of training and testing data, thereby enhancing the performance of the classification models. GANs are a specific framework of a generative model that aims to implicitly learn the data distribution from a set of samples to further generate new samples drawn from the learned distribution. The main idea behind GANs is that the generator network learns to produce data that resemble examples from a target data distribution. Synthetic data examples are generated to mimic real data using random noise as input [74].

The GAN comprises a generator and a discriminator, both of which are structured to facilitate efficient data generation and validation. The generator network starts with a feature input layer, followed by two fully connected layers and activation functions, resulting in a `tanh` layer to ensure the output ranges between -1 and 1. The discriminator network, on the other hand, includes a sequence of fully connected layers interspersed with leaky ReLU activations, ending in a sigmoid layer for binary classification. This setup enables the generator to create data samples that the discriminator evaluates, iteratively improving the quality of the generated data. Training involves normalizing the real data to the $[-1, 1]$ range and feeding noise through the generator to produce synthetic data. The discriminator then differentiates between real and generated data, computing losses that guide updates to both networks. Over 5000 epochs, this adversarial process refines the generator's ability to produce realistic data. The trained generator can then create new data samples, which are rescaled to match the range of the original data, demonstrating the effectiveness of the GAN in data synthesis. The samples of empty debris have been increased fivefold, using GAN to balance the number of samples compared to the other classes (respiration and movement).

To further validate the quality of the GAN-generated samples and their relevance to real measurements, we compared both the amplitude (Figure 8) and phase (Figure 9) of original and augmented noise signals. The time domain waveforms after DC removal reveal similar magnitudes and fluctuation patterns, indicating that the GAN effectively captures key statistical characteristics of the real signals. Figures 8 and 9 demonstrate that the synthetic data closely resemble real data while preserving key signal features. These visual confirmations, combined with our subsequent classification experiments, indicate that integrating GAN-augmented data not only balances class distributions but also preserves important signal features to improve overall model performance.

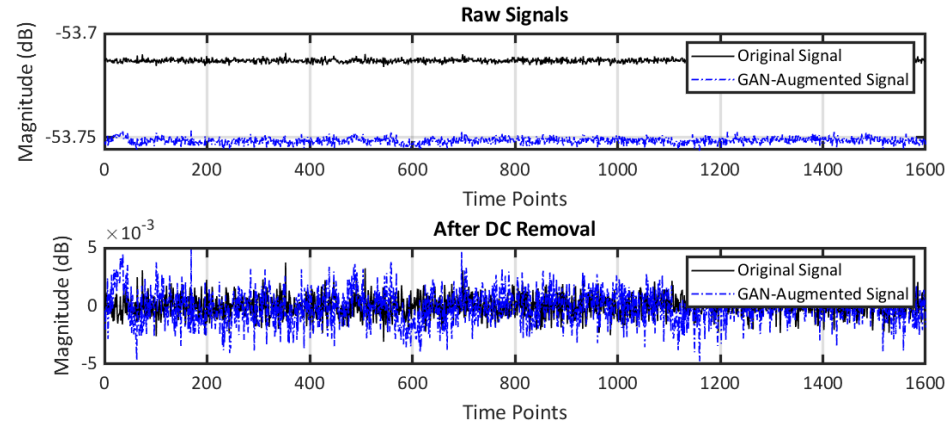


Figure 8. Comparison of original and GAN-augmented noise signals (Magnitude).

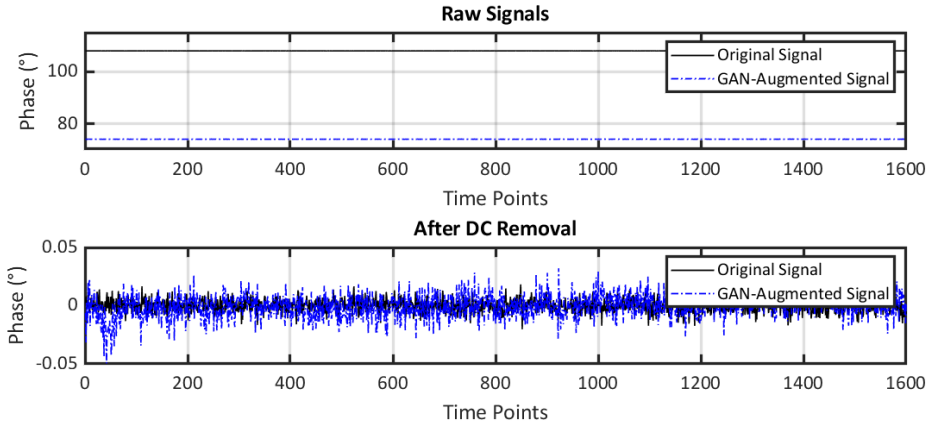


Figure 9. Comparison of original and GAN-augmented noise signals (Phase).

5. Deep Learning Models

In this work, AI-based classification techniques were employed to demonstrate the usability of the acquired data set. Signals recorded over time under debris were processed using LSTM, CNN, and TCN architectures without feature extraction. The principles of the networks are explained briefly, together with the parameters used in this work for human detection.

5.1. Long Short-Term Memory

Recurrent neural networks (RNNs) offer a valuable advantage in their ability to incorporate the surrounding context while connecting input and output sequences. To overcome the challenge of gradients diminishing over time in RNNs, LSTM was introduced [75]. The LSTM structure comprises interconnected subnetworks referred to as memory blocks, which are similar to memory chips in a computer but differentiable. Each block encompasses self-connected memory cells and three multiplicative units (the input, output, and forget gates), mimicking continuous versions of write, read, and reset operations for the cells. In essence, an LSTM memory block, illustrated in Figure 10, comprises a single cell. An LSTM network resembles a standard RNN, except that the traditional summation units in the hidden layer are replaced by memory blocks, as depicted in Figure 10b. While LSTM blocks can be combined with regular summation units, it is often unnecessary. Furthermore, the same output layers applicable to standard RNNs can be utilized for LSTM networks [76].

In this work, the model was optimized using a random search method across the hyper-parameter ranges detailed in Table 3 through 100 iterations. To construct AI models, subsets were allocated 80% for training, 10% for testing, and 10% for validation purposes. During the validation phase, random search hyper-parameter optimization was performed over all iterations using a parameter space defined by epoch, mini batch size, gradient threshold, initial learn rate, drop factor, and drop period, yielding customized network models tailored to achieve the best data fit. The epoch refers to the number of times the entire data set passes through the network during training. Mini batch size is the number of samples processed before the model is updated. Gradient threshold is a technique to prevent exploding gradients by capping the gradients during back-propagation. The initial learning rate determines the step size at each iteration while moving toward a minimum of the loss function. Drop factor is a factor by which the learning rate is reduced. Drop period is the number of epochs between reductions of the learning rate.

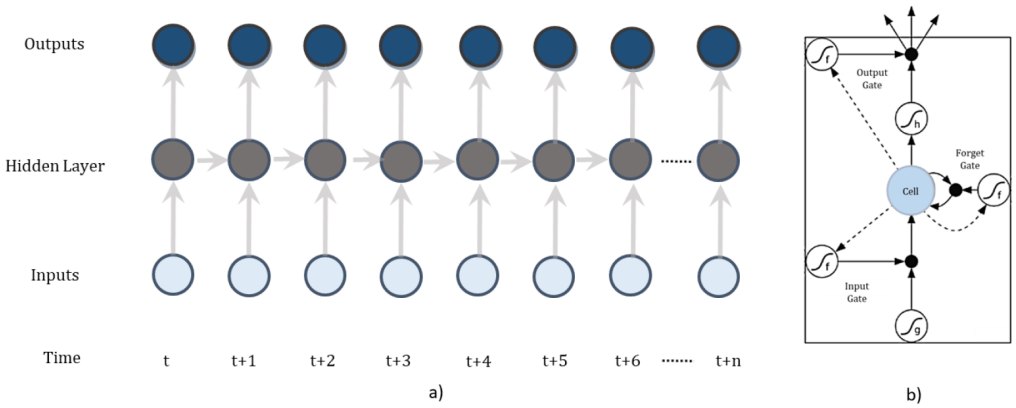


Figure 10. LSTM of original and GAN− : (**a**) Network. (**b**) Memory block with one cell.

Table 3. The hyper-parameter space of the LSTM.

Mini Batch Size	Hidden Units	Initial Learning Rate
1, 2, 4, 8	16, 32, 64, 128	0.001–0.1

5.2. Convolutional Neural Networks

The CNN is one of the most important networks in the field of DL and has been widely used across various domains in recent years. These networks, which exhibit high generalization ability for both 2D and 1D signals, achieve high classification accuracy when constructed with appropriate hyper-parameters. It is a feedforward neural network capable of feature extraction from data, a capability it achieves through convolutional structures. What sets CNN apart from traditional methods is its lack of reliance on feature engineering. Inspired by the visual perception of living organisms, the design of CNN incorporates artificial neurons resembling biological neurons, which are associated with CNN kernels representing different receptors. Activation functions symbolize functions capable of transmitting neuron signals that surpass a certain threshold. Loss and cost functions have been developed to determine the learning objectives of the CNN system. Creating a CNN model typically requires four main components. Convolution, the fundamental step of feature extraction, is utilized to obtain feature maps, with these maps being the outputs of convolutional kernels. When a specific convolution kernel size is determined, if there is a risk of information loss at the edge regions, the input is padded with zero values to expand it. Additionally, to control the density of convolution, a stride is used, where larger strides can lead to decreased density. Following convolution, pooling structures are employed to prevent over-fitting, including maximum pooling and average pooling,

among others [77]. To construct a CNN model, in this work, subsets were allocated 80% for training, 10% for testing, and 10% for validation. During the validation phase, random search hyper-parameter optimization was performed over 100 iterations. Test samples were separated using a holdout partition, while the validation data split was evaluated using nine-fold cross-validation. This optimization utilized a parameter space defined by filter sizes, hidden units, learning rates, and mini-batch sizes, each for shaping the architecture of CNNs. Filter sizes, ranging from 2 to 128, determined the dimensions of the convolutional kernels, affecting the receptive field and feature extraction. Hidden units, with options of 16, 32, 64, or 128, specified the number of neurons in each hidden layer. Learning rates between 0.001 and 0.1 controlled the step size for the optimization algorithm. Mini-batch sizes, from one to eight, defined the number of samples used per iteration, affecting training as detailed in Table 4. By exploring this parameter space through random search optimization, customized CNN models were developed using the topology given in Figure 11 to achieve optimal performance.

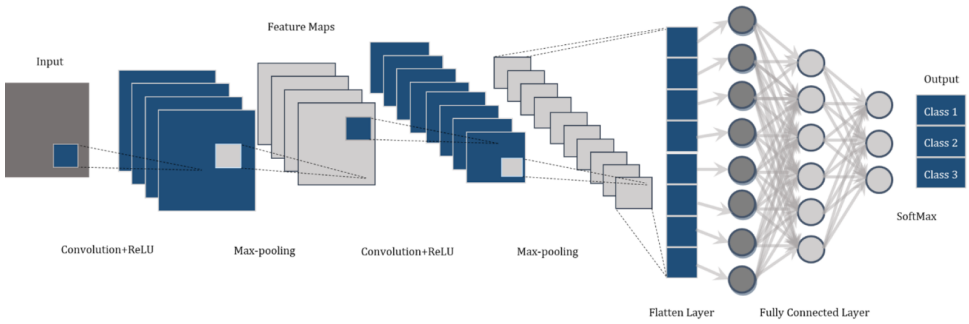


Figure 11. Convolutional neural network topology.

Table 4. The hyper-parameter space of the CNN.

Size of the Filters	Hidden Units	Learning Rates	Mini Batch Size
2, 4, 8, 16, 32, 64, 128	16, 32, 64, 128	0.001–0.1	1, 2, 4, 8

5.3. Temporal Convolutional Networks

TCNs, one-dimensional CNN architectures, utilize a temporal convolutional layer that operates on the steps of each time series. In this context, "temporal" implies that the activations calculated for a specific time step are independent of future time steps. Multiple convolutional layers are often added together to establish context from previous time steps. The dilation factor of consecutive convolutional layers increases exponentially to achieve larger receptive field sizes. The general structure of a TCN consists of a series of residual blocks. Each block comprises two sets of dilated temporal convolutional layers with the same dilation factor. Following these layers, normalization, ReLU activation function, and spatial dropout layers are applied. The network aggregates the output of each block with the input of the block, ultimately obtaining the output by applying an activation function [78].

To construct the AI models, subsets were allocated 80% for training, 10% for validation, and 10% for testing. During the validation phase, random search hyper-parameter optimization was performed over 100 iterations using a parameter space defined by Table 5. As in [79], a sequence-to-one approach was used for the surrogate model in this work. In constructing TCNs, key parameters included dilation factors for capturing long-range dependencies, filter sizes for temporal extent, number of filters for feature depth, dropout

rates for preventing over-fitting, mini batch size for training efficiency, and an optimizer for parameter updates.

Table 5. The hyper-parameter space of the TCN.

Dilation Factors	Size of the Filters	Number of Filters	Dropout Rates	Mini Batch Size	Optimizer
1–16	2–16	2, 4, 8, 16, 32, 64	0.1–0.8	1, 2, 4, 8	Adam

6. Results

The data set generated using the UWB bistatic radar system on the debris model was used to demonstrate the classification performance of the AI for human breathing and movement detection. An HP W10Pro workstation with Intel XEON W-1250 4.7GHz processor, 128 GB RAM, 512GB SSD, RTX A2000 GPU was used. Accuracy analyses of the classifier algorithms were tested for three different cases: "empty/respiration", "empty/movement," and "empty/respiration/movement." While the first two problems have two classes with 240 samples, the last problem is evaluated in three classes with 360 samples. The results indicate that DL models can be considered a promising approach for this problem.

6.1. Evaluation of Performance Metrics

Accuracy, precision, recall, and F1 score—the most informative and frequently used metrics to evaluate classifiers—were used as the performance metrics. Accuracy is a performance metric that serves as a fundamental metric in classification tasks, representing the proportion of correctly classified instances among the total number of instances, as given in Equation (4) [80]. Precision, given in Equation (5), is a measure of the exactness of a classifier, reflecting the proportion of true positive predictions among all instances predicted as positive. Recall assesses the completeness of a classifier, indicating the proportion of true positive predictions among all actual positive instances as given in Equation (6). F1 score harmonizes precision and recall, offering a comprehensive assessment of a classifier's performance by considering the balance between the two metrics, as given in Equation (7).

$$\text{Accuracy} = \frac{\text{TP} + \text{TN}}{\text{TP} + \text{TN} + \text{FP} + \text{FN}}; \tag{4}$$

$$\text{Precision} = \frac{\text{TP}}{\text{TP} + \text{FP}}; \tag{5}$$

$$\text{Recall} = \frac{\text{TP}}{\text{TP} + \text{FN}}; \tag{6}$$

$$\text{F1 Score} = 2 \times \frac{\text{Precision} \times \text{Recall}}{\text{Precision} + \text{Recall}}. \tag{7}$$

The confusion matrices presented in Figures 12 and 13 provide an integrated view of correctly and incorrectly predicted classes, highlighting patterns of overlap among empty debris, respiration, and movement signals. In particular, respiration and slight body movements can produce similar low-amplitude micro-motion signatures, making them prone to misclassification under noisy conditions. For example, minor torso shifts or interference from external vibrations may resemble breathing patterns, thereby confusing the model's learned features.

In examining our available data in Figures 12 and 13, we notice that respiration and movement signals occasionally exhibit overlapping characteristics, especially in the low-amplitude range. Slight variations in breathing or minor body movements can appear

highly similar, leading to misclassification even in controlled tests. This observation underscores the difficulty of reliably distinguishing these signals in real-world scenarios, where environmental noise and subtle human motions can blur the boundary between respiration and movement signatures. Table 6 presents the performance metrics of different DL models across various classification tasks involving empty, respiration, and movement classes at three different frequencies.

Table 6. Performance metrics of different DL models across various classification tasks.

ID	Problem	Freq. [MHz]	Classifier	Precision	Recall	F1 Score	Accuracy
1	Empty-Respiration	210	TCN	0.66	0.89	0.76	0.79
			LSTM	0.81	0.9	0.86	0.87
			CNN (STFT)	0.92	1	0.96	0.96
			CNN (CWT)	0.9	0.9	0.91	0.92
2	Empty-Movement	210	TCN	1	0.89	0.94	0.96
			LSTM	1	1	1	1
			CNN (STFT)	1	0.92	0.96	0.96
			CNN (CWT)	1	1	1	1
3	Empty-Respiration-Movement	210	TCN	0.89	0.89	0.89	0.89
			LSTM	0.84	0.83	0.83	0.86
			CNN (STFT)	*	*	*	*
			CNN (CWT)	*	*	*	*
4	Empty-Respiration	332.5	TCN	1	0.85	0.92	0.92
			LSTM	1	1	1	1
			CNN (STFT)	1	0.92	0.96	0.96
			CNN (CWT)	1	0.91	0.95	0.95
5	Empty-Movement	332.5	TCN	1	1	1	1
			LSTM	0.9	0.91	0.91	0.92
			CNN (STFT)	1	1	1	1
			CNN (CWT)	1	1	1	1
6	Empty-Respiration-Movement	332.5	TCN	0.9	0.92	0.9	0.92
			LSTM	0.74	0.8	0.74	0.75
			CNN (STFT)	*	*	*	*
			CNN (CWT)	*	*	*	*
7	Empty-Respiration	405	TCN	1	0.92	0.96	0.96
			LSTM	1	1	1	1
			CNN (STFT)	0.92	0.92	0.92	0.92
			CNN (CWT)	0.92	0.92	0.92	0.92
8	Empty-Movement	405	TCN	1	1	1	1
			LSTM	1	1	1	1
			CNN (STFT)	1	1	1	1
			CNN (CWT)	1	1	1	1
9	Empty-Respiration-Movement	405	TCN	0.97	0.97	0.97	0.97
			LSTM	0.84	0.75	0.76	0.78
			CNN (STFT)	*	*	*	*
			CNN (CWT)	*	*	*	*

* The performance metrics could not be established due to the high demand for workstation memory.

6.2. Classification Results

The results presented in Table 7 highlight notable differences in performance among various classification methods. Overall, CNN-based approaches (STFT and CWT) achieve the highest accuracy for certain problem types, while TCN (EMD) and LSTM (EMD) methods exhibit lower performance under specific conditions. Additionally, variations in problem definitions and frequency settings significantly impact model performance.

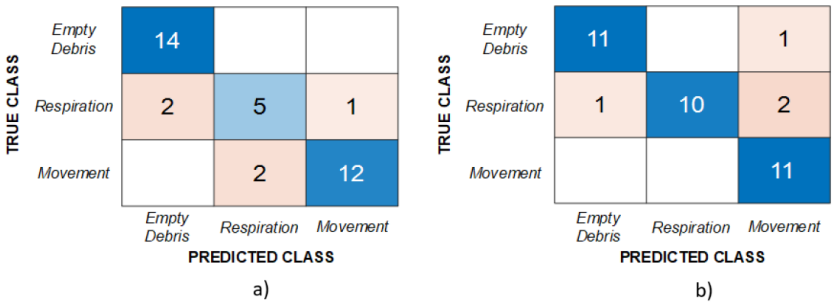


Figure 12. Confusion matrices of the DL models for Subset 3: (**a**) LSTM. (**b**) TCN.

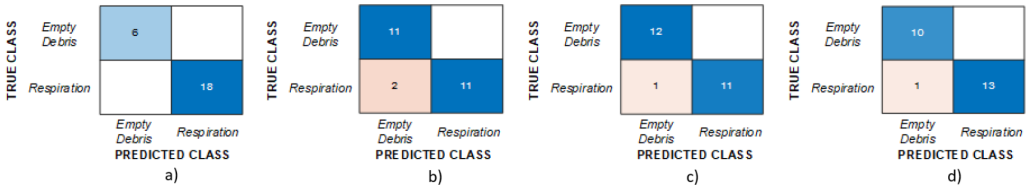


Figure 13. Confusion matrices of the DL models for Subset 4: (**a**) LSTM. (**b**) TCN. (**c**) CNN (with STFT data). (**d**) CNN (with CWT data).

For the empty/respiration classification task, the CNN (STFT) method outperforms the others, achieving the highest accuracy in both validation (94.17%) and test (95.83%) phases. In contrast, the TCN (EMD) model exhibits the lowest accuracy (validation: 80.06%, test: 79.17%), indicating a weaker capacity for distinguishing between empty and respiration classes. This trend persists across different frequency settings, although the LSTM (EMD) model reaches 100% accuracy in certain conditions (e.g., 332.5 MHz test phase), demonstrating its potential under specific circumstances.

For the empty/movement classification, both CNN (STFT) and CNN (CWT) achieve perfect accuracy (100%) across validation and test phases. Interestingly, at 405 MHz, all methods reach 100% accuracy, whereas at 210 MHz, the TCN (EMD) model exhibits the lowest validation accuracy (72.98%), while LSTM (EMD) and CNN-based methods maintain superior performance (100%). This discrepancy suggests that some methods struggle with movement detection at lower frequencies but significantly improve at higher frequencies.

The empty/respiration/movement classification task, which involves a more complex three-class distinction, reveals a more pronounced difference in model performance. At 405 MHz, the TCN (EMD) model achieves a relatively high test accuracy (97.22%), whereas LSTM (EMD) performs considerably worse (77.78%). Notably, CNN-based approaches could not produce results due to excessive memory demands, indicating potential computational inefficiencies when handling multi-class classification with these methods.

In general, the empty/movement task exhibits the highest overall classification accuracy across models, while the empty/respiration/movement task, particularly for LSTM (EMD), demonstrates the lowest performance. CNN-based methods tend to achieve higher accuracy, whereas the TCN (EMD) model appears to be more sensitive to frequency variations, exhibiting the lowest accuracy in certain scenarios. However, the absence of detailed error breakdowns limits interpretability, particularly for misclassification analysis in more complex classification tasks. Consequently, identifying the underlying factors contributing to misclassifications remains challenging, which could impact the generalizability of these models in real-world applications.

Table 7. Classification results of DL models.

ID	Problem	Class 1	Class 2	Class 3	# of Samples	Freq. [MHz]	Phase	TCN (EMD) [%]	LSTM (EMD) [%]	CNN (STFT) [%]	CNN (CWT) [%]
1	Empty-Respiration	Empty	Respiration	–	240	210	Validation	80.06	89.52	94.17	84.49
							Test	79.17	87.50	95.83	91.67
2	Empty-Movement	Empty	Movement	–	240	210	Validation	72.98	97.12	100.00	100.00
							Test	95.83	100.00	95.83	100.00
3	Empty-Respiration-Movement	Empty	Respiration	Movement	360	210	Validation	87.50	74.44	*	*
							Test	88.89	86.11	*	*
4	Empty-Respiration	Empty	Respiration	–	240	332.5	Validation	94.98	93.35	97.91	96.25
							Test	91.67	100.00	95.83	95.83
5	Empty-Movement	Empty	Movement	–	240	332.5	Validation	82.51	97.53	100.00	99.59
							Test	100.00	91.67	100.00	100.00
6	Empty-Respiration-Movement	Empty	Respiration	Movement	360	332.5	Validation	91.39	75.28	*	*
							Test	91.67	75.00	*	*
7	Empty-Respiration	Empty	Respiration	–	240	405	Validation	93.76	85.77	97.94	95.01
							Test	95.83	91.67	100.00	91.67
8	Empty-Movement	Empty	Movement	–	240	405	Validation	100.00	100.00	100.00	100.00
							Test	100.00	100.00	100.00	100.00
9	Empty-Respiration-Movement	Empty	Respiration	Movement	360	405	Validation	90.56	68.33	*	*
							Test	97.22	77.78	*	*

* The performance metrics could not be established due to the high demand for workstation memory.

7. Discussion

This work introduces a novel methodology for respiration detection in real rubble environments, centered on the utilization of time-dependent transmission coefficients from UWB radar signals operating in the 150–650 MHz range. In particular, three well-established signal processing transformations—STFT, WT, and EMD—are integrated with deep learning frameworks to enhance classification performance. The proposed approach aims to accurately discriminate among three classes (empty/respiration/movement) while maintaining low computational overhead. Comparative analyses indicate that these signal processing methods significantly affect classification outcomes, underscoring the importance of carefully selecting data transformations in conjunction with deep neural architectures.

Extensive evaluations have been carried out using TCN, LSTM, and CNN models across multiple frequency ranges and transformation techniques. The resulting performance metrics show that CNN architectures, especially those combined with STFT, yield high classification accuracy under various scenarios.

Nonetheless, memory and computational demands become critical considerations when CNNs are applied in multi-class settings. In contrast, TCN and LSTM show variable behaviors: TCN's performance, particularly when paired with EMD, may decline at lower frequencies, possibly due to challenges in capturing the subtle time–frequency patterns. LSTM demonstrates the capability to achieve state-of-the-art accuracy at specific frequency bands but encounters difficulties in multi-class tasks, possibly due to inefficient handling of extended sequence dependencies.

Another noteworthy outcome of the present study is the identification of misclassifications that occur with increasing task complexity, such as distinguishing among empty, respiration, and movement conditions. The lack of fine-grained error analysis impedes a deeper understanding of which specific class pairs are more prone to confusion. Analyzing such misclassification patterns—especially to ascertain the degree to which respiration signals might be mistaken for movement under certain conditions—would provide valuable insights for refining model architectures and data processing pipelines. Addressing these intricacies is vital to improving classification reliability and ensuring that the proposed framework generalizes well to a broad spectrum of real-world scenarios.

In the context of this study, a single type of rubble environment was created under laboratory conditions, and multiple individuals were positioned at various angles and postures to generate distinct signal types (respiration and movement). These signals were then analyzed using LSTM, CNN, and TCN models to assess classification performance. While the findings demonstrate promising results in detecting different human activities within this controlled setup, real-world deployments pose further challenges. Future research endeavors will broaden the experimental scope to include diverse and realistic debris scenarios, which may introduce additional signal variations and complexities. This progression toward more varied settings aims to ensure that the proposed methodology evolves into a robust, efficient, and reliable system for detecting and classifying respiration-related signals across a wide range of practical—and potentially harsh—environments.

Consequently, while the laboratory setup is realistic, the absence of field testing in actual post-disaster environments limits the generalizability of the findings. However, as part of our planned future work, we will conduct extensive real-world testing in controlled post-disaster environments with varied debris compositions, noise conditions, and environmental interferences. These experiments will validate the robustness of our approach and refine the model's adaptability to practical search and rescue scenarios, ensuring its effectiveness in real-world systems deployed in emergency situations.

Author Contributions: Conceptualization, Ö.N., M.Z.E., A.S.T., S.A.C., B.E. and N.T.T.; methodology, Ö.N., M.Z.E., A.S.T., S.A.C., B.E. and N.T.T.; software, Ö.N. and M.Z.E.; validation, Ö.N., M.Z.E., A.S.T., S.A.C., B.E. and N.T.T.; formal analysis, Ö.N., M.Z.E., A.S.T., S.A.C., B.E. and N.T.T.; investigation, Ö.N., M.Z.E., A.S.T., S.A.C., B.E. and N.T.T.; resources, A.S.T., S.A.C., B.E. and N.T.T.; data curation, Ö.N., M.Z.E., A.S.T., S.A.C., B.E. and N.T.T.; writing—original draft preparation, Ö.N. and M.Z.E.; writing—review and editing, A.S.T., S.A.C., B.E. and N.T.T.; visualization, Ö.N. and M.Z.E.; supervision, A.S.T., B.E. and N.T.T.; project administration, N.T.T.; funding acquisition, N.T.T. All authors have read and agreed to the published version of the manuscript.

Funding: This work was supported by The Scientific and Technological Research Council of Türkiye (Project Number: 121E409).

Institutional Review Board Statement: The study is approved by the Ethics Committee of Yıldız Technical University (2021/08 and 15 October 2021).

Informed Consent Statement: Informed consent was obtained from all subjects involved in the study.

Data Availability Statement: The datasets presented in this article are not readily available because the data are part of an ongoing study.

Conflicts of Interest: The authors declare no conflicts of interest.

Abbreviations

The following abbreviations are used in this manuscript:

AAC	Autoclaved Aerated Concrete
AD	Arctangent Demodulation
ANN	Artificial Neural Network
ATM	Advanced Template Matching
CSD	Complex Signal Demodulation
CNN	Convolutional Neural Network
DL	Deep Learning
DNN	Deep Neural Network
EMD	Empirical Mode Decomposition
FFT	Fast Fourier Transform
FT	Fourier Transform
GAN	Generative Adversarial Network
LSTM	Long Short-Term Memory
STFT	Short-Time Fourier Transform
TCN	Temporal Convolutional Network
UWB	Ultra-Wideband
VMD	Variational Mode Decomposition
VNA	Vector Network Analyzer
WT	Wavelet Transform

References

1. Agapiou, A.; Mikedi, K.; Karma, S.; Giotaki, Z.K.; Kolostoumbis, D.; Papageorgiou, C.; Zorba, E.; Spiliopoulou, C.; Amann, A.; Statheropoulos, M. Physiology and biochemistry of human subjects during entrapment. *J. Breath Res.* **2013**, *7*, 016004.
2. Statheropoulos, M.; Agapiou, A.; Pallis, G.C.; Mikedi, K.; Karma, S.; Vamvakari, J.; D.; oulaki, M.; Andritsos, F.; Thomas, C.P. Factors that affect rescue time in urban search and rescue (USAR) operations. *Nat. Hazards* **2015**, *75*, 57–69.
3. Yoncacı, İ. Development of a Road Map and Emergency Help and Detection System for Disaster Search and Rescue Operations. Ph.D. Thesis, Middle East Technical University, Ankara, Türkiye, 2020.
4. Zhang, Z.; You, J.; Li, Q.; Du, X. Research Framework for Emergency Rescue of Disasters and Crises. *J. Risk Anal. Crisis Response* **2021**, *2*, 3.
5. Thavasi, P.T.; Suriyakala, C.D. Sensors and Tracking Methods Used in Wireless Sensor Network-Based Unmanned Search and Rescue System—A Review. *Procedia Eng.* **2012**, *38*, 1935–1945.

6. Shah, S.A.; Fioranelli, F. RF Sensing Technologies for Assisted Daily Living in Healthcare: A Comprehensive Review. *IEEE Aerosp. Electron. Syst. Mag.* **2019**, *34*, 26–44.
7. Sujatmiko, W.; Prastio, R.P.; Danudirdjo, D.; Suksmono, A.B. A Review of Radars to Detect Survivors Buried Under Earthquake Rubble. In Proceedings of the 5th International Conference on Instrumentation, Communications, Information Technology, and Biomedical Engineering (ICICI-BME), Bandung, Indonesia, 6–7 November 2017; pp. 309–313.
8. Uzunidis, D.; Mitilineos, S.A.; Ponti, C.; Schettini, G.; Patrikakis, C.Z. Detection of trapped victims behind large obstacles using radar sensors: A review on available technologies and candidate solutions. In Proceedings of the IEEE Conference on Antenna Measurements and Applications (CAMA), Genoa, Italy, 15–17 November 2023; pp. 1025–1030.
9. Rong, Y.; Gutierrez, R.; Mishra, K.V.; Bliss, D.W. Noncontact Vital Sign Detection With UAV-Borne Radars: An Overview of Recent Advances. *IEEE Veh. Technol. Mag.* **2021**, *16*, 118–128.
10. Haddad, W.S. *The Rubble Rescue Radar (RRR): A Low Power Hand-Held Microwave Device for the Detection of Trapped Human Personnel*; UCRL-ID–127786; Lawrence Livermore National Lab.(LLNL): Livermore, CA, USA , 1997.
11. Lv, H.; Li, W.; Li, Z.; Zhang, Y.; Jiao, T.; Xue, H.; Liu, M.; Jing, X.; Wang, J. Characterization and Identification of IR-UWB Respiratory-Motion Response of Trapped Victims. *IEEE Trans. Geosci. Remote Sens.* **2014**, *52*, 7195–7204. https://doi.org/10.1109/TGRS.2014.2309141.
12. Liang, X.; Zhang, H.; Fang, G.; Ye, S.; Gulliver, T.A. An Improved Algorithm for Through-Wall Target Detection Using Ultra-Wideband Impulse Radar. *IEEE Access* **2017**, *5*, 22101–22118. https://doi.org/10.1109/ACCESS.2017.2761771.
13. Arai, I. Survivor search radar system for persons trapped under earthquake rubble. In Proceedings of the APMC 2001. 2001 Asia-Pacific Microwave Conference, Taipei, Taiwan, 3–6 December 2001; Volume 2, pp. 663–668. https://doi.org/10.1109/APMC.2001.985460.
14. Denoual, J.M.; Floc'h, J.M.; Mutzig, J.P.; Massaloux, P.; Ducasse, F.; Minvielle, P.; Labarthe, C. Design of two flare UWB antenna dedicated to the research of alive buried victims. In Proceedings of the 40th European Microwave Conference, Paris, France, 28–30 September 2010; pp. 1710–1713. https://doi.org/10.23919/EUMC.2010.5616967.
15. Koo, Y.S.; Ren, L.; Wang, Y.; Fathy, A.E. UWB MicroDoppler Radar for human Gait analysis, tracking more than one person, and vital sign detection of moving persons. In Proceedings of the 2013 IEEE MTT-S International Microwave Symposium Digest (MTT), Seattle, WA, USA, 2–7 June 2013; pp. 1–4. https://doi.org/10.1109/MWSYM.2013.6697702.
16. Rittiplang, A.; Phasukkit, P. UWB Radar for Multiple Human Detection Through the Wall Based on Doppler Frequency and Variance Statistic. In Proceedings of the 2019 12th Biomedical Engineering International Conference (BMEiCON), Ubon Ratchathani, Thailand, 19–22 November 2019; pp. 1–5. https://doi.org/10.1109/BMEiCON47515.2019.8990358.
17. Zaikov, E.; Sachs, J.; Aftanas, M.; Rovnakova, J. Detection of trapped people by UWB radar. In Proceedings of the German Microwave Conference, Hamburg, Germany, 10–12 March 2008; pp. 1–4.
18. Labarthe, C.; Mutzig, J.P.; Jecko, B.; Hamieh, H.; Martinod, E.; Feix, N.; Lal, e J.M.; Denoual, J.M.; Floch, J.M.; Bertr, V.; et al. An Ultra-Wideband radar concept for the detection of buried victims beneath building rubble. In Proceedings of the 2009 International Radar Conference "Surveillance for a Safer World" (RADAR 2009), Bordeaux, France, 12–16 October 2009; pp. 1–6.
19. Baboli, M.; Boric-Lubecke, O.; Lubecke, V. A new algorithm for detection of heart and respiration rate with UWB signals. In Proceedings of the 2012 Annual International Conference of the IEEE Engineering in Medicine and Biology Society, San Diego, CA, USA, 28 August–1 September 2012; pp. 3947–3950. https://doi.org/10.1109/EMBC.2012.6346830.
20. Zhang, Z.; Zhang, X.; Lv, H.; Lu, G.; Jing, X.; Wang, J. Human-Target Detection and Surrounding Structure Estimation Under a Simulated Rubble via UWB Radar. *IEEE Geosci. Remote Sens. Lett.* **2013**, *10*, 328–331. https://doi.org/10.1109/LGRS.2012.2205555.
21. Stavrou, S.; Saunders, S.R. Review of constitutive parameters of building materials. In Proceedings of the Twelfth International Conference on Antennas and Propagation (ICAP 2003), Exeter, UK, 31 March–3 April 2003; Volume 1, pp. 211–215. https://doi.org/10.1049/cp:20030052.
22. Shen, Y.-H.; Chien, Y.-R.; Fang, S.-H. Human detection with weak ranging signal for FMCW radar systems. In Proceedings of the 19th ACM/IEEE International Conference on Information Processing in Sensor Networks (IPSN), Sydney, NSW, Australia, 21–24 April 2020; pp. 343–344.
23. Shi, D.; Liang, F.; Qiao, J.; Wang, Y.; Zhu, Y.; Lv, H.; Yu, X.; Jiao, T.; Liao, F.; Yan, K.; et al. A Novel Non-Contact Detection and Identification Method for the Post-Disaster Compression State of Injured Individuals Using UWB Bio-Radar. *Bioengineering* **2023**, *10*, 905. https://doi.org/10.3390/bioengineering10080905.
24. Wang, C.; Zhang, Y.; Xie, T.; Guo, L.; Chen, S.; Li, J.; Shi, F. A Detection Method for Collapsed Buildings Combining Post-Earthquake High-Resolution Optical and Synthetic Aperture Radar Images. *Remote Sens.* **2022**, *14*, 1100. https://doi.org/10.3390/rs14051100.
25. Nezirovic, A.; Yarovoy, A. G.; Ligthart, L. P. Signal Processing for Improved Detection of Trapped Victims Using UWB Radar. *IEEE Trans. Geosci. Remote Sens.* **2010**, *48*, 2005–2014. https://doi.org/10.1109/TGRS.2009.2036840.

26. Yang, S.; Qin, H.; Liang, X.; Gulliver, T.A. Clutter Elimination and Harmonic Suppression of Non-Stationary Life Signs for Long-Range and Through-Wall Human Subject Detection Using Spectral Kurtosis Analysis (SKA)-Based Windowed Fourier Transform (WFT) Method. *Appl. Sci.* **2019**, *9*, 355. https://doi.org/10.3390/app9020355.
27. Chernyak, V. Detection problem for searching survivors in rubble with UWB radars. In Proceedings of the 2008 European Radar Conference, Amsterdam, The Netherlands, 30–31 October 2008; pp. 44–47.
28. Wacker, M.; Witte, H. Time-Frequency Techniques in Biomedical Signal Analysis: A Tutorial Review of Similarities and Differences. *Methods Inf. Med.* **2013**, *52*, 279–296. https://doi.org/10.3414/ME12-01-0083
29. Valizadeh, G.; Babapour Mofrad, F. A Comprehensive Survey on Two and Three-Dimensional Fourier Shape Descriptors: Biomedical Applications. *Arch. Comput. Methods Eng.* **2022**, *29*, 4643–4681. https://doi.org/10.1007/s11831-022-09750-7
30. Granados-Lieberman, D.; Huerta-Rosales, J.R.; Gonzalez-Cordoba, J.L.; Amezquita-Sanchez, J.P.; Valtierra-Rodriguez, M.; Camarena-Martinez, D. Time-Frequency Analysis and Neural Networks for Detecting Short-Circuited Turns in Transformers in Both Transient and Steady-State Regimes Using Vibration Signals. *Appl. Sci.* **2023**, *13*, 12218. https://doi.org/10.3390/app132212218
31. Urbina Fredes, S.; Dehghan Firoozabadi, A.; Adasme, P.; Zabala-Blanco, D.; Palacios Játiva, P.; Azurdia-Meza, C. Enhanced Epileptic Seizure Detection through Wavelet-Based Analysis of EEG Signal Processing. *Appl. Sci.* **2024**, *14*, 5783. https://doi.org/10.3390/app14135783
32. Baboli, M.; Ghorashi, S.A.; Saniei, N.; Ahmadian, A. A New Wavelet-Based Algorithm for Estimating Respiratory Motion Rate Using UWB Radar. In Proceedings of the 2009 International Conference on Biomedical and Pharmaceutical Engineering (ICBPE), Singapore, 2–4 December 2009; pp. 1–3. https://doi.org/10.1109/ICBPE.2009.5384095
33. Kamble, H.; Phadke, G.S. Frequency Response Analysis of Respiratory Sounds and Comparative Study for Windowing Techniques. In Proceedings of the 2016 International Conference on Signal Processing, Communication, Power and Embedded System (SCOPES), Paralakhemundi, India, 3–5 October 2016; pp. 210–215. https://doi.org/10.1109/SCOPES.2016.7955809.
34. Liang, X.; Zhang, H.; Ye, S.; Fang, G.; Gulliver, T.A. Improved denoising method for through-wall vital sign detection using UWB impulse radar. *Digit. Signal Process.* **2018**, *74*, 72–93. https://doi.org/10.1016/j.dsp.2017.12.004.
35. Gouveia, C.; Albuquerque, D.; Pinho, P.; Vieira, J. Evaluation of Heartbeat Signal Extraction Methods Using a 5.8 GHz Doppler Radar System in a Real Application Scenario. *IEEE Sensors J.* **2022**, *22*, 7979–7989. https://doi.org/10.1109/JSEN.2022.3156474.
36. Weishaupt, F.; Walterscheid, I.; Biallawons, O.; Klare, J. Vital Sign Localization and Measurement Using an LFMCW MIMO Radar. In Proceedings of the 2018 19th International Radar Symposium (IRS), Bonn, Germany, 20–22 June 2018; pp. 1–8. https://doi.org/10.23919/IRS.2018.8448229.
37. Xu, H.; Liu, J.; Hu, H.; Zhang, Y. Wearable Sensor-Based Human Activity Recognition Method with Multi-Features Extracted from Hilbert-Huang Transform. *Sensors* **2016**, *16*, 2048. https://doi.org/10.3390/s16122048.
38. Narayanan, R. M. Earthquake survivor detection using life signals from radar micro-Doppler. In Proceedings of the ACWR '11: Proceedings of the 1st International Conference on Wireless Technologies for Humanitarian Relief, Kerala, India, 18–21 December 2011; pp. 259–264. https://doi.org/10.1145/2185216.2185288.
39. Mišić, N.Ž.; Ostojić, M.; Cvetković, S.; Miodragović, P.; Aničić, Z.; Kovačić Popović, A.; Stefanović, Đ. Wavelet Analysis of Respiratory Muscle sEMG Signals during the Physiological Breakpoint of Static Dry End-Expiratory Breath-Holding in Naive Apneists: A Pilot Study. *Sensors* **2023**, *23*, 7200. https://doi.org/10.3390/s23167200.
40. Campolo, M.; Labate, D.; La Foresta, F.; Morabito, F.C.; Lay-Ekuakille, A.; Vergallo, P. ECG-derived respiratory signal using Empirical Mode Decomposition. In Proceedings of the 2011 IEEE International Symposium on Medical Measurements and Applications (MeMeA), Bari, Italy, 30–31 May 2011; pp. 399–403. https://doi.org/10.1109/MeMeA.2011.5966727.
41. Rasheed, A.; Veluvolu, K.C. Respiratory Motion Prediction with Empirical Mode Decomposition-Based Random Vector Functional Link. *Mathematics* **2024**, *12*, 588. https://doi.org/10.3390/math12040588.
42. Ding, C.; Yan, J.; Zhang, L.; Zhao, H.; Hong, H.; Zhu, X. Noncontact multiple targets vital sign detection based on VMD algorithm. In Proceedings of the 2017 IEEE Radar Conference (RadarConf), Seattle, WA, USA, 8–12 May 2017; pp. 727–730. https://doi.org/10.1109/RADAR.2017.7944298.
43. Liang, J.; Zhang, Y.; Guo, S.; Cui, G. Improved Method of Human Vital Sign Parameters Estimation Based on Hilbert-Huang Transform. In Proceedings of the 2021 CIE International Conference on Radar (Radar), Haikou, China, 15–19 December 2021; pp. 3069–3073. https://doi.org/10.1109/Radar53847.2021.10028033.
44. Ren, L.; Wang, H.; Naishadham, K.; Kilic, O.; Fathy, A. Phase-based methods for heart rate detection using UWB impulse Doppler radar. *IEEE Trans. Microw. Theory Tech.* **2016**, *64*, 3319–3331. https://doi.org/10.1109/TMTT.2016.2597824.
45. Will, C.; Shi, K.; Schellenberger, S.; Steigleder, T.; Michler, F.; Fuchs, J.; Weigel, R.; Ostgathe, C.; Koelpin, A. Radar-based heart sound detection. *Sci. Rep.* **2018**, *8*, 11551. https://doi.org/10.1038/s41598-018-29984-5.
46. Nijsure, Y.; Tay, W.P.; Gunawan, E.; Wen, F.; Yang, Z.; Guan, Y.L.; Chua, A.P. An impulse radio ultrawideband system for contactless noninvasive respiratory monitoring. *IEEE Trans. Biomed. Eng.* **2013**, *60*, 1509–1517. https://doi.org/10.1109/TBME.2012.2237401.

47. Lai, J.; Xu, Y.; Gunawan, E.; Chua, E.C.; Maskooki, A.; Guan, Y.L.; Low, K.S.; Soh, C.B.; Poh, C.L. Wireless sensing of human respiratory parameters by low-power ultrawideband impulse radio radar. *IEEE Trans. Instrum. Meas.* **2011**, *60*, 928–938. https://doi.org/10.1109/TIM.2010.2064370.
48. Tu, J.; Hwang, T.; Lin, J. Respiration rate measurement under 1-D body motion using single continuous-wave Doppler radar vital sign detection system. *IEEE Trans. Microw. Theory Tech.* **2016**, *64*, 1937–1946. https://doi.org/10.1109/TMTT.2016.2560159.
49. Li, J.; Zeng, Z.; Sun, J.; Liu, F. Through-wall detection of human being's movement by UWB radar. *IEEE Geosci. Remote Sens. Lett.* **2012**, *9*, 1079–1083. https://doi.org/10.1109/LGRS.2012.2190707.
50. Shirodkar, S.; Barua, P.; Anuradha, D.; Kuloor, R. Heart-beat detection and ranging through a wall using ultra wide band radar. In Proceedings of the 2011 International Conference on Communications and Signal Processing, Kerala, India, 10–12 February 2011; pp. 579–583. https://doi.org/10.1109/ICCSP.2011.5739391.
51. Applications of artificial intelligence techniques in engineering. In *Advances in Intelligent Systems and Computing*; Springer: Berlin/Heidelberg, Germany , 2019. https://doi.org/10.1007/978-981-13-1822-1.
52. Niyaz, Ö.; Tüylü, T.; Mahouti, P.; Erkmen, B.; Tokan, N. T. Detection and classification of human respiration under building debris model using VHF/UHF waves. *Neural Comput. Appl.* **2024**, *36*, 1–17.
53. Yang, Y.; Yuan, Y.; Zhang, G.; Wang, H.; Chen, Y.C.; Liu, Y.; Tarolli, C.G.; Crepeau, D.; Bukartyk, J.; Junna, M.R.; et al. Artificial intelligence-enabled detection and assessment of Parkinson's disease using nocturnal breathing signals. *Nat. Med.* **2022**, *28*, 2207–2215. https://doi.org/10.1038/s41591-022-01932-x.
54. Zeng, X.; Robakowski, J.; Persson, M.; Monteith, A.; Fhager, A. Investigation of an Ultra Wideband Noise Sensor for Health Monitoring. *Sensors* **2020**, *20*, 1034. https://doi.org/10.3390/s20041034.
55. Sim, J.Y.; Park, J.-H.; Yang, J.-R. Vital-Signs Detector Based on Frequency-Shift Keying Radar. *Sensors* **2020**, *20*, 5516. https://doi.org/10.3390/s20195516.
56. Yu, C.; Xu, Z.; Yan, K.; Chien, Y.-R.; Fang, S.-H.; Wu, H.-C. Noninvasive Human Activity Recognition Using Millimeter-Wave Radar. *IEEE Syst. J.* **2022**, *16*, 3036–3047. https://doi.org/10.1109/JSYST.2022.3140546.
57. Oliveira, M. L. L. de.; Bekooij, M. Deep convolutional autoencoder applied for noise reduction in range-Doppler maps of FMCW radars. In Proceedings of the 2020 IEEE International Radar Conference (RADAR), Washington, DC, USA, 28–30 April 2020; pp. 630–635. https://doi.org/10.1109/RADAR42522.2020.9114719.
58. Malešević, N.; Petrović, V.; Belić, M.; Antfolk, C.; Mihajlović, V.; Janković, M. Contactless Real-Time Heartbeat Detection via 24 GHz Continuous-Wave Doppler Radar Using Artificial Neural Networks. *Sensors* **2020**, *20*, 2351. https://doi.org/10.3390/s20082351.
59. Chuma, E.L.; Iano, Y. A Movement Detection System Using Continuous-Wave Doppler Radar Sensor and Convolutional Neural Network to Detect Cough and Other Gestures. *IEEE Sensors J.* **2021**, *21*, 2921–2928. https://doi.org/10.1109/JSEN.2020.3028494.
60. Choi, S.H.; Yoon, H. Convolutional Neural Networks for the Real-Time Monitoring of Vital Signs Based on Impulse Radio Ultrawide-Band Radar during Sleep. *Sensors* **2023**, *23*, 3116. https://doi.org/10.3390/s23063116.
61. Shi, C.; Zheng, Z.; Pan, J.; Ni, Z.K.; Ye, S.; Fang, G. Multiple Stationary Human Targets Detection in Through-Wall UWB Radar Based on Convolutional Neural Network. *Appl. Sci.* **2022**, *12*, 4720. https://doi.org/10.3390/app12094720.
62. Han-Trong, T.; Nguyen Viet, H. An efficient heart rate measurement system using medical radar and LSTM Neural Network. *J. Electr. Comput. Eng.* **2022**, *2022*, 4696163. https://doi.org/10.1155/2022/4696163.
63. Ariffin, F.S.; Kamarudin, L.M.; Ghazali, N.; Nishizaki, H.; Zakaria, A.; bin, Syed, Zakaria, S.M.M. Inhalation and exhalation detection for sleep and awake activities using Non-Contact ultra-wideband (UWB) radar signal. *J. Physics: Conf. Ser.* **2021**, *1755*, 012038. https://doi.org/10.1088/1742-6596/1755/1/012038.
64. Liu, L.B.; Liu, M.; Wang, J.Q. Electromagnetic environment comprehension for radar detection of vital signs at China National Training Center for earthquake search & rescue. In Proceedings of the 2016 16th International Conference on Ground Penetrating Radar (GPR), Hong Kong, China, 13–16 June 2016; pp. 1–4. https://doi.org/10.1109/ICGPR.2016.7572667.
65. Li, Z.; Jin, T.; Li, L.; Dai, Y.; Song, Y.; Song, Y.; Zhou, X. Spatiotemporal Processing for Remote Sensing of Trapped Victims Using 4-D Imaging Radar. *IEEE Trans. Geosci. Remote Sens.* **2023**, *61*, 5103412. https://doi.org/10.1109/TGRS.2023.3266039.
66. An, Q.; Zhang, X.; He, Y.; Yang, J.; Liu, B. Wavelet-Based Human Target Detection in Complex Ruins Using a Low Center Frequency UWB Radar. In Proceedings of the 2016 Progress in Electromagnetic Research Symposium (PIERS), Shanghai, China, 8–11 August 2016; pp. 1744–1747. https://doi.org/10.1109/PIERS.2016.7734777.
67. Li, Z.; Jing, X.; Li, W.; Wang, J. A Wavelet-Based Strong Clutter Removal Technique for UWB Life Detection. In Proceedings of the 2012 14th International Conference on Ground Penetrating Radar (GPR), Shanghai, China, 4–8 June 2012; pp. 957–960. https://doi.org/10.1109/ICGPR.2012.6255001.
68. Kumar, A.; Tomar, H.; Mehla, V. K.; Komaragiri, R.; Kumar, M. Stationary wavelet transform based ECG signal denoising method. *ISA Trans.* **2021**, *114*, 251–262. https://doi.org/10.1016/j.isatra.2020.12.029.
69. MathWorks. MATLAB Wavelet Toolbox. Getting Started Guide. MathWorks, 2016. Available online: https://www.mathworks.com/help/wavelet/ (accessed on 1 September 2024).

70. Pradhan, B.K.; Neelappu, B.C.; Sivaraman, J.; Kim, D.; Pal, K. A Review on the Applications of Time-Frequency Methods in ECG Analysis. *J. Healthc. Eng.* **2023**, *2023*, 3145483. https://doi.org/10.1155/2023/3145483.
71. Huang, N.E.; Attoh-Okine, N.O. *The Hilbert-Huang Transform in Engineering*; CRC Press: Boca Raton, FL, USA, 2005; pp. 100–111.
72. Junsheng, C.; Dejie, Y.; Yu, Y. Research on the intrinsic mode function (IMF) criterion in EMD method. *Mech. Syst. Signal Process.* **2006**, *20*, 817–824.
73. Zhu, Z.; Yang, D.; Zhao, R.; Liang, B. Vital Sign Signal Extraction Method Based on Permutation Entropy and EMD Algorithm for Ultra-Wideband Radar. In Proceedings of the 2019 3rd International Conference on Electronic Information Technology and Computer Engineering (EITCE), Xiamen, China, 18–20 October 2019; pp. 1268–1273. https://doi.org/10.1109/EITCE47263.2019.9094801.
74. Goodfellow, I.; Pouget-Abadie, J.; Mirza, M.; Xu, B.; Warde-Farley, D.; Ozair, S.; Courville, A.; Bengio, Y. Generative adversarial nets. *Adv. Neural Inf. Process. Syst.* **2014**. Available online: https://proceedings.neurips.cc/paper_files/paper/2014/file/5ca3e9b122f61f8f06494c97b1afccf3-Paper.pdf (accessed on 1 September 2024).
75. Hochreiter, S.; Schmidhuber, J. Long Short-Term Memory. *Neural Comput.* **1997**, *9*, 1735–1780.
76. Graves, A. Long Short-Term Memory. In *Supervised Sequence Labelling with Recurrent Neural Networks. Studies in Computational Intelligence*; Springer: Berlin/Heidelberg, Germany, 2012; Volume 385.
77. Li, Z.; Liu, F.; Yang, W.; Peng, S.; Zhou, J. A survey of Convolutional Neural Networks: Analysis, applications, and prospects. *IEEE Trans. Neural Networks Learn. Syst.* **2022**, *33*, 6999–7019. https://doi.org/10.1109/tnnls.2021.3084827.
78. Bai, S.; Kolter, J. Z.; Koltun, V. An Empirical Evaluation of Generic Convolutional and Recurrent Networks for Sequence Modeling. *arXiv*, **2018**. https://arxiv.org/abs/1803.01271.
79. Lea, C.; Vidal, R.; Reiter, A.; Hager, G.D. Temporal Convolutional Networks: A Unified Approach to Action Segmentation. In *Computer Vision—ECCV 2016 Workshops. ECCV 2016*; Lecture Notes in Computer Science; Hua, G., Jégou, H., Eds.; Springer: Cham, Switzerland, 2016; Volume 9915.
80. Akila, B.; Nayahi, J. J. V. Parkinson classification neural network with mass algorithm for processing speech signals. *Neural Comput. Appl.* **2024**, *36*, 10165–10181.

Disclaimer/Publisher's Note: The statements, opinions and data contained in all publications are solely those of the individual author(s) and contributor(s) and not of MDPI and/or the editor(s). MDPI and/or the editor(s) disclaim responsibility for any injury to people or property resulting from any ideas, methods, instructions or products referred to in the content.